Lattice dynamics of beryllium oxide: Inelastic x-ray scattering and *ab initio* calculations

Alexey Bosak,[1] Karin Schmalzl,[2] Michael Krisch,[1] Wouter van Beek,[3,4] and Vitaly Kolobanov[5]
[1]*European Synchrotron Radiation Facility, Boîte Postale 220, 38043 Grenoble Cedex, France*
[2]*Institut für Festkörperforschung, Forschungszentrum Jülich GmbH, Jülich Centre for Neutron Science at ILL, 38042 Grenoble Cedex 9, France*
[3]*Swiss-Norwegian Beamlines, ESRF, Boîte Postale 220, 38043 Grenoble Cedex, France*
[4]*Dipartamento di Scienze e Tecnologie Avanzate, Universita del Piemonte Orientale and NanoSistemi IC, Via Bellini 25/G, I-15100 Alessandria, Italy*
[5]*Faculty of Physics, Moscow State University, 119992 Moscow, Russia*
(Received 15 April 2008; published 12 June 2008)

The phonon-dispersion relations of the lightest wurtzite structure compound BeO have been determined from inelastic x-ray scattering (IXS) measurements and analyzed by *ab initio* calculations. Experimental data and calculations show good agreement and reconcile the existing controversies. The phonon linewidth of the longitudinal-optical phonon along Γ-*A* reveals a marked *q* dependence, which can be correlated with the two-phonon density of states, thus pointing toward a strong anharmonic behavior.

DOI: 10.1103/PhysRevB.77.224303 PACS number(s): 63.20.D−, 61.05.cf, 71.15.Mb, 62.20.D−

I. INTRODUCTION

Bromellite BeO is the only alkaline-earth mono-oxide crystallizing in the wurtzite structure, instead of the NaCl-type structure (for Mg, Ca, Sr, and Ba), and is the lightest representative of the wurtzite-structure family. Noteworthy, this material is close to being isotopically pure as Be has only one natural isotope and natural oxygen contains 99.8% of ^{16}O. It has found many applications due to its unusually high thermal conductivity (~3.7 W/cm K at room temperature and 137 W/cm K at 45 K),[1] high electrical resistivity (large direct gap of ~10.63 eV),[2] high bulk modulus, and high melting point. It has been used as a nuclear moderator and reflector material, as well as a heat sink for high-power applications.

The information on the lattice dynamics of BeO is limited to Raman[3–7] and IR-absorption[3] studies, and inelastic-neutron-scattering (INS) data for selected low-lying phonon branches.[8,9] The first INS study showed the presence of a nearly flat branch[9] at low energy not observed in a subsequent experiment.[8] More complete studies of the lattice dynamics of BeO, both experimental and theoretical, would help to address the above controversy and furthermore provide insight into the anharmonicity of BeO by a study of the phonon linewidth throughout the Brillouin zone. The aim of the present work therefore is to establish the complete phonon-dispersion relations for the totality of branches and confront it with *ab initio* calculations.

II. COMPUTATIONAL AND EXPERIMENTAL DETAILS

A. *Ab initio* calculation

BeO crystallizes in the wurtzite structure ($P6_3mc$) with two molecules in the hexagonal unit cell, with the Be atoms at the relative positions (0 0 0) and (1/3 2/3 1/2) and the O atoms at (0 0 *u*) and (1/3 2/3 *u*+1/2). The electronic and dynamical properties have been determined within the framework of density-functional theory (DFT) by employing the local-density approximation (LDA). For the calculations we have used the ABINIT code,[10] which gives direct access to various response functions that are second derivatives of the total energy with respect to different perturbations, such as phonon displacements or a static homogeneous electric field. The physical properties connected to these perturbations are the phonon dynamical matrices, the dielectric tensor, and the Born effective charges. For Be and O we have used Troullier–Martins (TM) pseudopotentials[11] which were taken from the ABINIT database. With this pseudopotential, static and dynamic properties are well reproduced.

The lattice constant has been determined from the numerical minimum of the total energy. A $6\times6\times4$ special *k*-point grid and a cut-off energy of E_{cut}=90 hartree (~2450 eV) have been found to be sufficient. Higher *k*-point grids of $8\times8\times4$ up to $10\times10\times10$ resulted all in lattice constants of

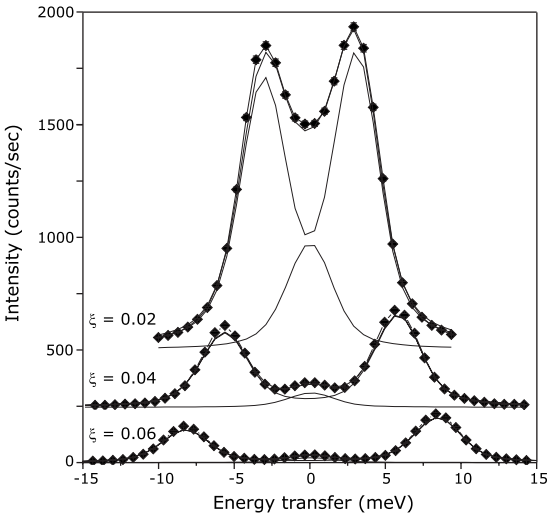

FIG. 1. Selected IXS spectra for the in-plane polarized transverse acoustic (TA) phonons propagating along Γ-*M* at the indicated *Q* values $(1+\xi\ 1-\xi\ 0)$, given in reciprocal-lattice vector units. The experimental data are shown together with the best fit results (solid lines). The spectra are shifted along the vertical direction for clarity, conserving the same intensity scale.

TABLE I. BeO: Calculated and experimental crystal structures and dielectric properties.

Method	a (Å)	c (Å)	u	$\varepsilon_{\infty}\perp_c$	$\varepsilon_{\infty}\|c$	Ref.
ABINIT (TM)	2.7141	4.4209	0.3771	3.0647	3.1236	Present
FLAPW (LDA)	2.6681	4.3461	0.38			12
U.S.-Psp. (LDA)	2.6459	4.2599	0.377		3.15	13
U.S.-Psp. (GGA)	2.701	4.387	0.3777			14
Exp. (300 K)	2.6979(2)	4.3772(2)	0.378			15
Exp. (300 K)				2.95	2.99	3

a=2.7141 Å and c=4.4209 Å with u=0.3771.

The calculated lattice constants from different approaches and programs are listed in Table I together with experimental values. The results of the different calculations coincide quite well; but, as already seen in many other cases, our LDA plane-wave calculation overestimates the value of the experimental lattice parameter, whereas other calculations, also performed in LDA, underestimate it. The deviation of our calculation from the experimental value is less than 1% in a and c.

The lattice-dynamics calculations were performed within the linear-response approach (see, e.g., Ref. 16), as implemented in the ABINIT program. For our calculations of the phonon dispersion, a cut-off energy E_{cut} of 90 hartree (~2450 eV) and a special k-point mesh of $6\times6\times4$ has been used, as in the calculation of the lattice constant. No differences in the resulting frequencies were found for a k-point mesh of $8\times8\times8$ and a cut-off energy E_{cut} of 120 hartree (~3265 eV). The components of the high-frequency dielectric tensor yield 3.0647 in the basal plane and 3.1236 in the c direction, which are comparable to the results of the LDA calculation with ultrasoft pseudopotentials[13] and with results from infrared spectra[3] (see Table I). The components of the Born effective charges tensor result in −1.787 for oxygen in the basal plane and −1.845 in the c direction. A full-potential linearized augmented plane-wave (FLAPW) calculation[12] yields −1.72 for oxygen along the c direction.

The relatively large number of phonon branches (12) makes it necessary to use *a priori* lattice-dynamics calculations for the planning of the experiment and disentanglement of measured branches. (Q-E) maps were calculated for all the employed Brillouin zones using a standard formalism for $S(\vec{Q},E)$ within the limit of one-phonon scattering:[17]

$$S(\vec{Q},E)=\sum_j G(\vec{Q},j)F(E,T,\vec{Q},j), \tag{1}$$

with

$$G(\vec{Q},j)=\left|\sum_n f_n(\vec{Q})e^{-W_n(\vec{Q})+i\vec{Q}\cdot\vec{r}_n}[\vec{Q}\cdot\hat{\sigma}_n(\vec{q},j)]M_n^{-1/2}\right|^2, \tag{2}$$

and the thermal factor

$$F(E,T,\vec{Q},j)=\frac{\left\{\left[\exp\left(\frac{E_{\vec{q},j}}{kT}\right)-1\right]^{-1}+\frac{1}{2}\pm\frac{1}{2}\right\}}{E_{\vec{q},j}}\delta(E\mp E_{\vec{q},j}), \tag{3}$$

where $\vec{Q}=\vec{q}+\vec{\tau}$ denotes the momentum transfer. The sum extends over atoms in the unit cell; $f_n(\vec{Q})=f_n(|\vec{Q}|)\equiv f_n(Q)$ is the atomic form factor of atom n, $\hat{\sigma}_n(\vec{q}+\vec{\tau},j)=\hat{\sigma}_n(\vec{q},j)$ is its eigenvector component in mode j, M_n is its mass, and W_n is the corresponding Debye–Waller factor.[18]

B. Inelastic x-ray scattering measurements

The inelastic x-ray scattering (IXS) experiment was performed on beamline ID28 at the European Synchrotron Radiation Facility. The instrument was operated at 15 816 and

TABLE II. Summary of the investigated acoustic branches, indicating the direction of the total momentum transfer Q, the propagation and polarization vectors of the phonon, and the derived apparent sound velocity. The parameter ξ is always positive; polarization vectors for quasilongitudinal (qLA) and quasitransverse (qTA) phonon branches are not indicated.

	Notation	Momentum transfer	Propagation vector	Polarization vector	Velocity (km/s)
(1)	LA[1 1 0]	$[1-\xi\ 1-\xi\ 0]$	[1 1 0]	⟨1 1 0⟩	12.31(12)
(2)	LA[0 0 1]	$[0\ 0\ 2+\xi]$	[0 0 1]	⟨0 0 1⟩	12.76(13)
(3)	$TA[1\ 0\ 0]_{\langle001\rangle}$	$[\xi\ 0\ 2]$	[1 0 0]	⟨0 0 1⟩	7.19(7)
(4)	$TA[1\ 0\ 0]_{\langle1-20\rangle}$	$[1+\xi\ 1-\xi\ 0]$	$[\bar{1}10]$	⟨1 1 0⟩	7.85(8)
(5)	qLA[2 0 3]	$[1+2\xi\ 0\ 1+3\xi]$	[2 0 3]		12.01(12)
(6)	qTA[2 0 3]	$[1+2\xi\ 0\ 1+3\xi]$	[2 0 3]		8.11(8)

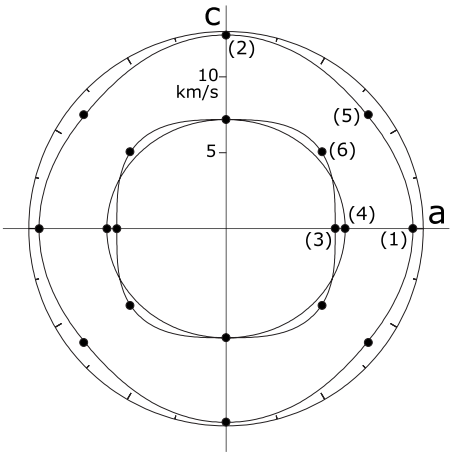

FIG. 2. Polar plot of the derived sound velocity data in the *a*-*c* plane: experimental data (points) and fit results (solid lines). Experimental points are enumerated as given in Table II.

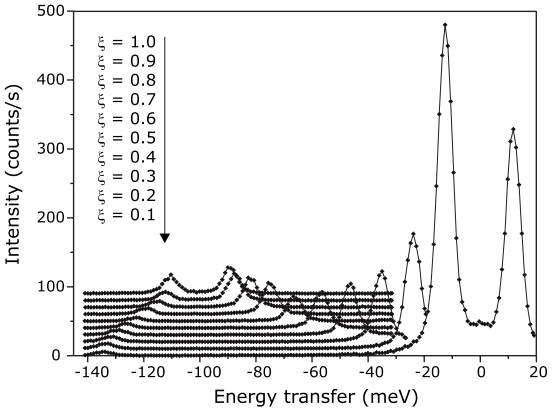

FIG. 3. IXS spectra for the longitudinal-acoustic (LA) and longitudinal-optic (LO) phonons propagating along Γ-*A* at the indicated *Q* values (0 0 2+ξ), given in reciprocal-lattice vector units. The spectra are shifted along the vertical direction by 10 cps for clarity, conserving the same intensity scale.

17 794 eV, providing overall energy resolutions of 6.0 and 3.0 meV full width at half maximum (FWHM), respectively. The direction and size of the momentum transfer were selected by an appropriate choice of the scattering angle and the sample orientation in the horizontal scattering plane. The momentum resolution was typically set to 0.25 (0.28) nm^{-1} and 0.75 (0.84) nm^{-1} in the horizontal and vertical planes, respectively, for the employed configurations. Further details of the experimental setup can be found elsewhere.[19] The examined BeO crystal was grown by Maslov *et al.*[20] by the advanced flux method. BeO crystals occurred in the form of plane-parallel plates with the natural facets oriented either parallel or perpendicular to the *c* axis. The dimensions of the focused x-ray beam were 250×60 μm^2 (horizontal $\times$ vertical, FWHM) and allowed us to select a single-crystal domain with a typical mosaic spread of about $\sim0.05°$ FWHM [for the (100) and (002) reflections]. The determined lattice parameters, $a=2.6977(5)$ Å and $c=4.3791(5)$ Å, are in good agreement with previous diffraction results [$a=2.6979(2)$ Å and $c=4.3772(2)$ Å (Ref. 15)] (see Table I as well).

C. Raman measurements

The Raman instrument used is a Renishaw inVia spectrometer specially adapted for remote measurements. The spectrometer is equipped with two different Raman lasers: a green (532 nm) laser and a red/near-infrared (NIR) (785 nm) laser. The dispersion is performed with a 1800 lines/mm grating for the 532 nm laser and a 1200 lines/mm grating for the 785 nm laser. Optical fibers distribute the exciting laser to the various instruments and a collection fiber returns the Raman signal to the spectrometer. An RP10 compact video fiber-optic probe with a 100 mm long-distance objective focuses the laser on the sample and collects the Raman signal back. The RP10 is equipped with edge filters to suppress Rayleigh scattering. The green laser was used for the BeO experiment.

III. RESULTS AND DISCUSSION

A. Elasticity

Acoustic phonons in the proximity of the Γ point were measured with 3 meV resolution. In Fig. 1 we report examples of the collected IXS spectra. These are characterized by a moderate elastic contribution centered at zero energy and two symmetric features, the Stokes and anti-Stokes peaks of the corresponding phonons. The energy position $E(q)$ of the phonons was extracted using a model function

TABLE III. Comparison of our results with previous experiments and theory. All values are in gigapascals.

	C_{11}	C_{12}	C_{13}	C_{33}	C_{44}	C_{66}	B
Present exp.	454(10)	85(16)	77(5)	488(10)	155(3)	185(4)	208(9)
Previous exp.	460.6[a]	126.5[a]	88.5[a]	491.6[a]	147.7[a]	167.0[a]	224[a]
	470[b]	168[b]	119[b]	494[b]	153[b]	152[b]	249[b]
							212(3)[c]
Theory[d]	439.1(3)	105(2)	72(1)	463(2)	142.1(5)	167(2)	204(1)

[a]Ultrasonic measurements (Ref. 21).
[b]Ultrasonic measurements (Ref. 22).
[c]Single-crystal x-ray diffraction (Ref. 23).
[d]DFT calculations (Ref. 14).

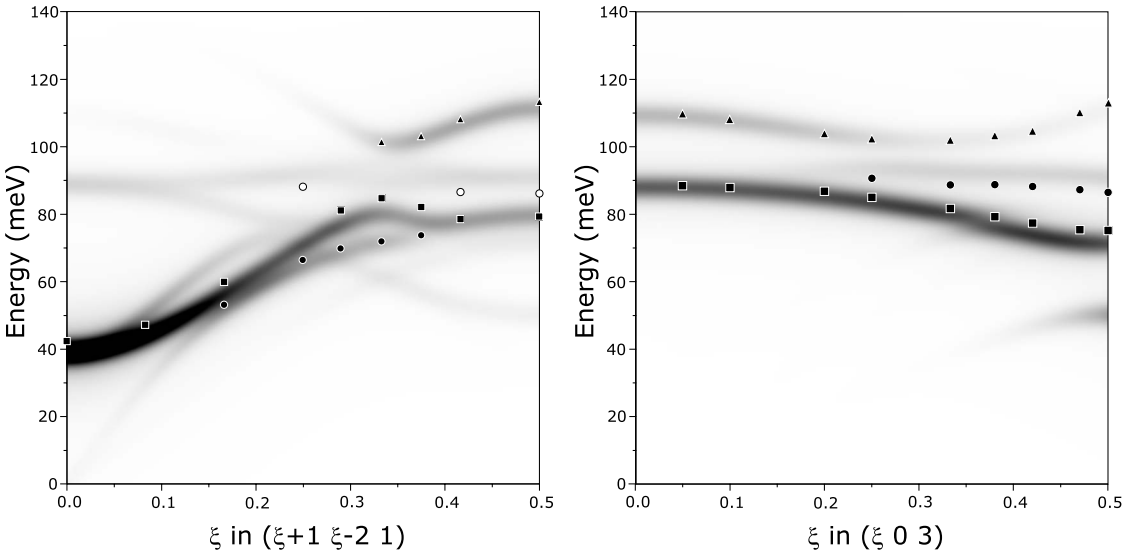

FIG. 4. Calculated intensity maps together with experimental phonon energies for Q regions ($\xi+1\ \xi-2\ 1$) and ($\xi\ 0\ 3$) with $0 \leq \xi \leq 0.5$. Identical symbols are attributed to the same branch.

composed of a sum of Lorentzian functions, for which the inelastic contributions were constrained by the Bose factor. This model function was convoluted with the experimentally determined resolution function and fitted to the IXS spectra, utilizing a standard χ^2 minimization routine. Typically, three to four q points along a specific crystallographic direction were used to extract the sound velocity. The sound velocity was derived from the slope of the acoustic phonon dispersion in the low q limit, in most cases by a linear or a sinusoidal fit $E(q)=A\ \sin(\pi q/B)$, formally equivalent to limiting the interatomic interactions to nearest neighbors (A and B denote constants).

Table II provides the list of investigated phonon branches and the corresponding derived sound velocities after correction of Q-resolution effects in a self-consistent way. The corresponding set of elastic moduli is reported in Table III, and the fitted sound velocities are presented in a polar plot in Fig. 2. Apart from C_{13} all other elastic moduli can be calculated directly from a single sound velocity, i.e., $C_{11}=\rho V(\mathrm{LA}[100])^2$, $C_{66}=\rho V(\mathrm{TA}[100]_{\langle 1-20\rangle})^2$, $C_{44}=\rho V(\mathrm{TA}[100]_{\langle 001\rangle})^2$, and $C_{33}=\rho V(\mathrm{LA}[001])^2$, where ρ is the density. C_{13} contributes to the sound velocity only for nonpure directions (i.e., neither in the equatorial plane nor along the axial direction).

Our results are in reasonable agreement with ultrasonic data[21] and previously performed first-principles calculation within the generalized gradient approximation of density-functional theory.[14] The bulk modulus derived from our data is also very close to the value obtained from a single-crystal compressibility experiment.[23] The largest deviations are found for C_{66} (and correspondingly for C_{12}).

B. Phonon dispersion

Phonons with energies higher than 20 meV were typically determined with an energy resolution of 6 meV. The high x-ray scattering power of BeO allowed us to reduce the acquisition time to 15 s/point even for high-energy optical phonons (see Fig. 3).

A thorough choice of the Brillouin zone was indispensable for the efficient data collection and consequent disentanglement of phonon branches. The ABINIT code[10] output was treated with specialized scripts developed under MATHCAD© in order to localize Brillouin zones, providing the highest intensity and the best contrast for a given phonon, and trace the intensity maps. An example of such maps together with the experimental points is presented in Fig. 4.

The majority of branches along high-symmetry directions Γ-A, Γ-M, and Γ-K-M could be traced throughout the Brillouin zone except for three branches along the Γ-K-M direction which could not be resolved with sufficient contrast due

TABLE IV. Fundamental Raman-active bands in BeO (energies in cm^{-1}).

	Ref. 3	Ref. 7	Ref. 6	Ref. 5	This work
E_2 (1)		337.6	338	338.5	337.3
A_1 (TO)		679.3	678		678
E_2 (2)	684	684.1	684	684.3	683
E_1 (TO)	725	723.9	722		722.7
A_1 (LO)	1085	1083.4	1081	1082.2	1080.6
E_1 (LO)	1095		1097		1095.6

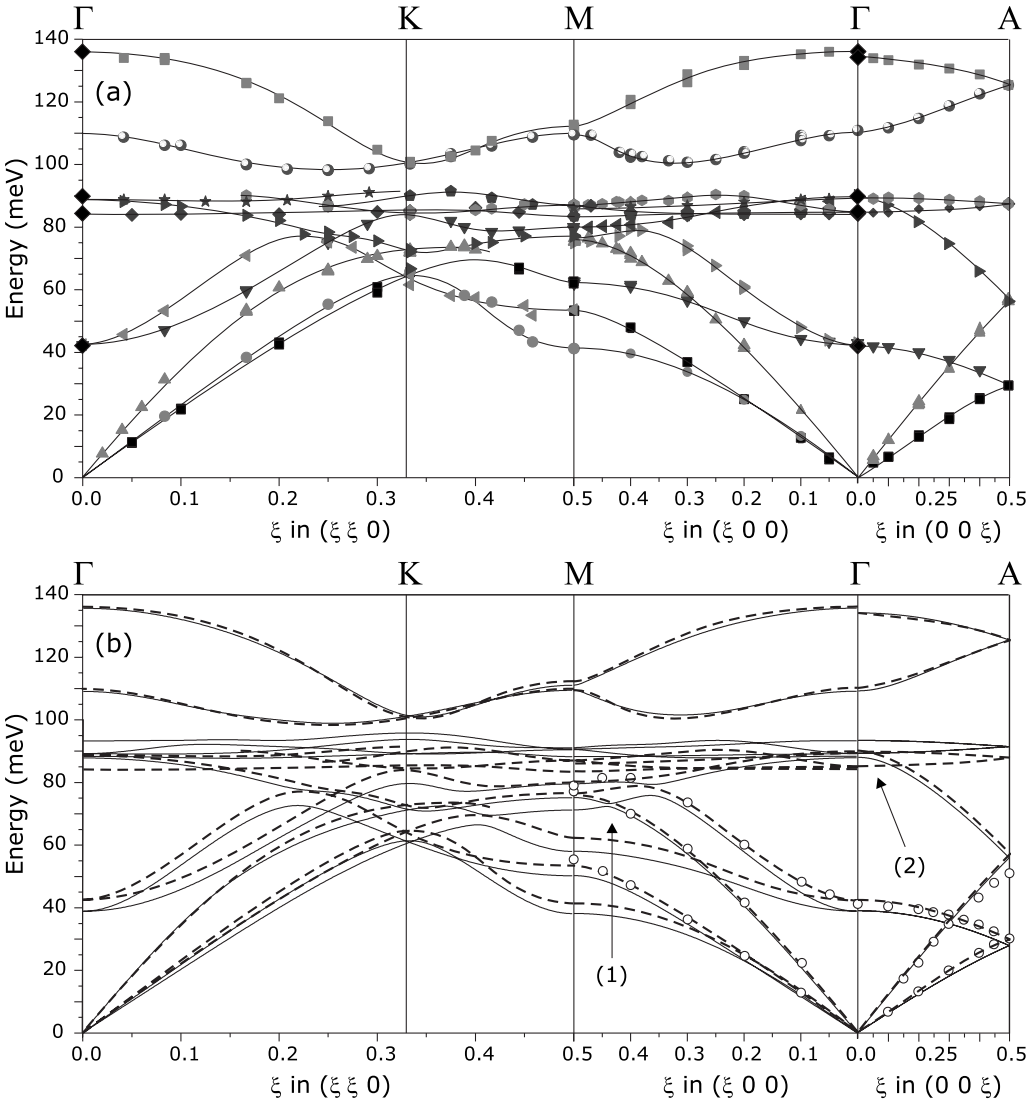

FIG. 5. Phonon dispersion for BeO along high-symmetry directions: (a) experimental points together with guides for the eye (Bézier curves); large diamonds correspond to Raman data (this work) and (b) comparison of our experimental dispersion (dashed lines) with *ab initio* calculation (solid lines) and INS data (Ref. 8) (empty circles).

to experimental constraints. Points belonging to the same branch are connected by Bézier curves for the facility of visualization. While the overall shape of the dispersion is nicely reproduced by our *ab initio* calculation, a series of low-energy branches are regularly lower in frequency. This could be explained by the utilized theoretical lattice parameters which are too large with respect to the experimental ones (see Table I). As a consequence, some qualitative differences appear: (i) the predicted anticrossing [Fig. 5(b), region 1] is actually absent and (ii) the order of Γ-point phonons is different [Fig. 5(b), region 2]. The absence of an anticrossing is also evidenced by the INS experiment of Ostheller *et al.*,[8] which provided low-energy branches closely coinciding with our IXS results. The absence of a flat branch in the range of 10–20 meV observed by Brugger *et al.*[9] is now definitely confirmed.

Beyond the complete determination of the phonon dispersion, we furthermore undertook a detailed study of the highest optical branches along the Γ-*A* direction with an energy resolution of 3 meV. The dynamical scattering factor $G(Q)$ was extracted [Fig. 6(a)], taking into account the scattering volume, polarization factor, and angular dependence of the analyzer efficiency. The calculated scattering factor uses mean-square displacements extracted from x-ray diffraction data.[18] A quite remarkable correspondence is observed. The increasing discrepancy toward larger ξ might be explained by a strongly anharmonic behavior, evidenced as well by the evolution of the phonon line width with ξ [Fig. 6(b)]. According to Ref. 5, the width of the highest optical mode is ~1.7 meV at room temperature, which nicely fits the IXS data. Further evidence for anharmonic behavior is obtained by the inspection of the two-phonon density of states, which shows a monotonous growth in the region of interest as illustrated by Fig. 6(c). To overcome the eventual possibility that the phonon width is sample dependent, we have repeated the Raman-scattering experiment on the same sample which has been used for IXS and the excess width for the LO phonon was found to be comparable with that found previously.[5]

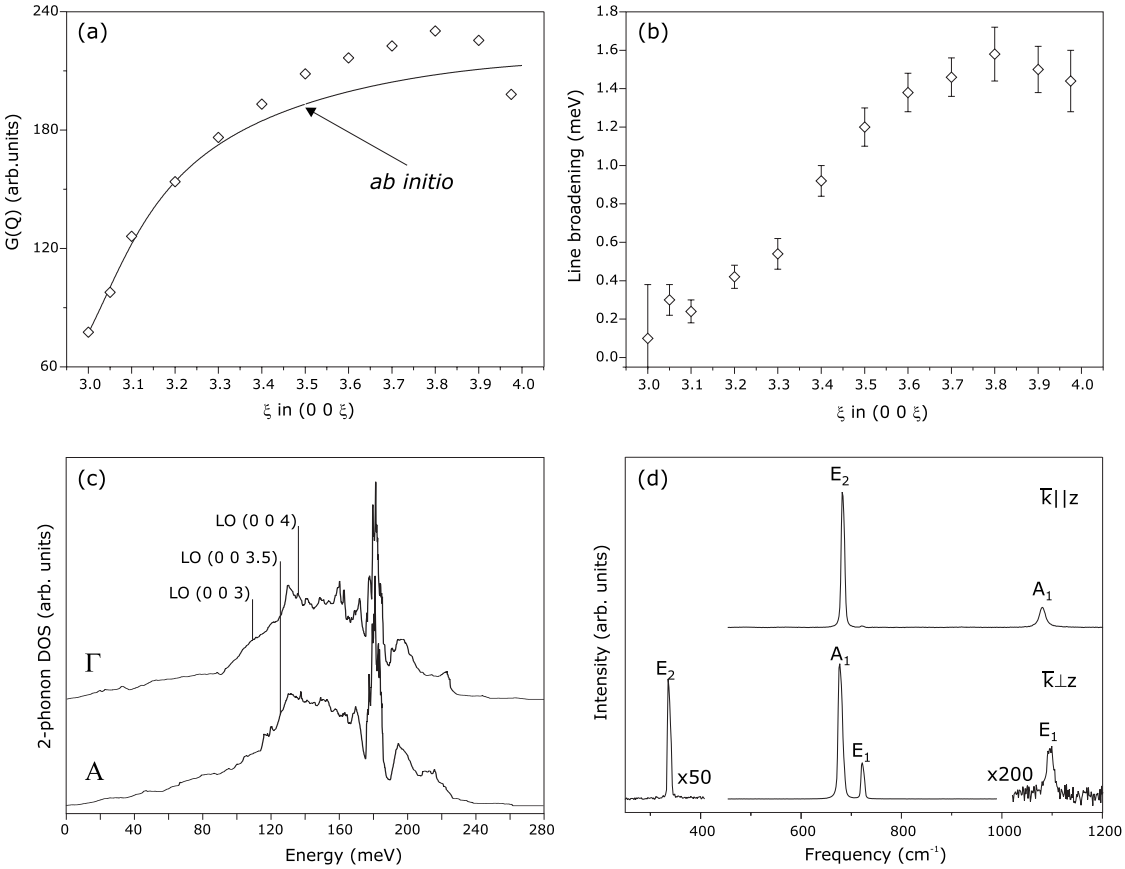

FIG. 6. (a) Dynamical structure factor $G(q)$ measured for the LO branch along the Γ-A direction (open diamonds) compared with *ab initio* calculation (solid line); (b) line broadening for the same branch; (c) *ab initio* calculated two-phonon density of states (DOS) (weighted by thermal occupation numbers) for Γ and A points with superposed LO frequencies at Γ and A points; (d) Raman spectra taken in two different configurations as indicated in the figure.

Examples of Raman spectra are given in Fig. 6(d); measurements in two configurations allowed us to extract all six fundamental frequencies reported in Table IV.

Our IXS and Raman observations and theoretical calculations are in very good agreement with previous reports.[3,5–7] While absolute energies are not exactly reproduced by the *ab initio* calculation, the theoretical E_1-A_1 splitting almost coincides with the experiment (5.5 meV vs 4.95 meV for TO and 1.9 meV vs 1.64 meV for LO). At the same time, the LO-TO splitting[24] is also reproduced in a reasonable way, giving $\varepsilon_{xx}^0/\varepsilon_{xx}^\infty=2.36$ and $\varepsilon_{zz}^0/\varepsilon_{zz}^\infty=2.06$, to be compared with the experimental values of 2.61 and 2.24, respectively.

IV. CONCLUSIONS

In summary, we have reported the phonon-dispersion relations of wurtzite BeO obtained by IXS and *ab initio* calculations. The IXS data are in good agreement with previously reported limited sets of INS and Raman data. Our *ab initio* calculations show an overall good agreement in the static as well as in the dynamical properties with minor discrepancies to the experimental phonon-dispersion data. As convergence was well achieved, discrepancies to experimental results might have its reason, e.g., in the used pseudopotential. The results achieved reconcile the existing controversies in the lattice-dynamics description of BeO.

[1] G. A. Slack and S. B. Austerman, J. Appl. Phys. **42**, 4713 (1971).
[2] D. M. Roessler, W. C. Walker, and E. Loh, J. Phys. Chem. Solids **30**, 157 (1969).
[3] E. Loh, Phys. Rev. **166**, 673 (1968).
[4] G. A. Kourouklis, A. K. Sood, H. D. Hochheimer, and A. Jayaraman, Phys. Rev. B **31**, 8332 (1985).
[5] G. Morell, W. Pérez, E. Ching-Prado, and R. S. Katiyar, Phys. Rev. B **53**, 5388 (1996).
[6] C. A. Arguello, D. L. Rousseau, and S. P. S. Porto, Phys. Rev. **181**, 1351 (1969).
[7] S. Devanarayanan, G. Morell, and R. S. Katiyar, J. Raman Spec-

trosc. **22**, 311 (1991).
[8] G. L. Ostheller, R. E. Schmunk, R. M. Brugger, and R. J. Kearney, *Inelastic Neutron Scattering* (IAEA, Vienna, 1968), p. 315.
[9] R. M. Brugger, K. A. Strong, and J. M. Carpenter, J. Phys. Chem. Solids **28**, 249 (1967).
[10] X. Gonze, Phys. Rev. B **55**, 10337 (1997); http://www.abinit.org
[11] N. Troullier and J. L. Martins, Phys. Rev. B **43**, 1993 (1991).
[12] A. Dal Corso, M. Posternak, R. Resta, and A. Baldereschi, Phys. Rev. B **50**, 10715 (1994).
[13] F. Bernardini and V. Fiorentini, Phys. Rev. B **58**, 15292 (1998).
[14] V. Milman and M. C. Warren, J. Phys.: Condens. Matter **13**, 241 (2001).
[15] J. W. Downs, F. K. Ross, and G. V. Gibbs, Acta Crystallogr., Sect. B: Struct. Sci. **41**, 425 (1985).
[16] S. Baroni, S. de Gironcoli, and A. Dal Corso, Rev. Mod. Phys. **73**, 515 (2001).
[17] E. Burkel, Rep. Prog. Phys. **63**, 171 (2000).
[18] G. Vidal-Valat, J. P. Vidal, K. Kurki-Suonio, and R. Kurki-Suonio, Acta Crystallogr., Sect. A: Found. Crystallogr. **43**, 540 (1987).
[19] M. Krisch and F. Sette, *Light Scattering in Solids, Novel Materials and Techniques*, Topics in Applied Physics No. 108 (Springer-Verlag, Berlin, 2007), p. 317.
[20] V. A. Maslov, G. M. Rylov, V. G. Mazurenko, A. V. Kruzhalov, and B. V. Shulgin, Proceedings of the Sixth International Conference on Crystal Growth, Moscow, 1980, Vol. 3, p. 286.
[21] C. F. Cline, H. L. Dunegan, and G. W. Henderson, J. Appl. Phys. **38**, 1944 (1967).
[22] G. G. Bentle, J. Am. Ceram. Soc. **49**, 125 (1966).
[23] R. M. Hazen and L. W. Finger, J. Appl. Phys. **59**, 3728 (1986).
[24] W. Cochran and R. A. Cowley, J. Phys. Chem. Solids **23**, 447 (1962).